



In vitro morphological profiling of T cells predicts clinical response to natalizumab therapy in patients with multiple sclerosis

Received: 5 June 2024

Accepted: 19 May 2025

Published online: 01 July 2025

Check for updates

Beatrix Chaves^{1,2,3}, Juan Carlo Santos e Silva^④, Helder Nakaya^⑤, Nicolas Socquet-Juglard¹, Florence Bucciarelli^{1,6}, Guilhèn Prunier¹, Matheus V. Almeida², Claire Lacouture¹, Saniya Kari^①, Anne L. Astier^①, Marco A. Medeiros^⑦, João H. M. Silva^{2,3}, Roland Liblau^{⑧,1}, Vinicius Cotta-de-Almeida^{⑨,10,12}✉ & Loïc Dupré^{①,11,12}✉

Despite the efficacy of natalizumab, which targets the integrin VLA-4, in treating multiple sclerosis (MS), approximately 35% patients with MS present evidence of disease activity two years after treatment initiation. Individual heterogeneity of leukocyte response to VLA-4 on natalizumab-mediated blockade may underlie disparities in treatment efficacy. Here we use a high-content cell imaging (HCI) pipeline to profile the in vitro effects of natalizumab on VLA-4-stimulated PBMCs from MS patients prior to natalizumab treatment. Unsupervised clustering of image data partially discriminates non-responder MS patients based on morphology, F-actin organization and signaling-related features in CD8⁺ T cells. Furthermore, through a random forest approach, treatment response can be predicted with a performance of 92% for a discovery cohort and 88% for a validation cohort. Unfavorable treatment response is associated with a distinct actin remodeling response of natalizumab-exposed CD8⁺ T cells and a residual ability of these cells to spread on VCAM-1. Our study thus unveils that CD8⁺ T cells from individual MS patients display heterogeneous susceptibility to natalizumab in vitro and highlights the potential of HCI-based pretreatment monitoring to assist individualized treatment prescription.

Very late antigen-4 (VLA-4) is a heterodimeric integrin composed of the $\alpha 4$ and $\beta 1$ subunits¹. VLA-4 mediates adhesion, transmigration and intra-tissue trafficking of immune cells, by interacting with vascular cell adhesion molecule-1 (VCAM-1) and fibronectin². In addition, this

integrin is involved in T-cell immune synapse assembly³ and activation^{4,5}. Because of its pivotal role in multiple aspects of T-cell biology, VLA-4 also contributes to mediate dysregulated T-cell responses, such as those underlying inflammatory diseases⁶.

¹Toulouse Institute for Infectious and Inflammatory Diseases (INFINITY), INSERM U1291, CNRS UMR5051, Toulouse University, Toulouse, France. ²Structural and Functional Biology of Biopharmaceuticals, Fiocruz-Ceará, Oswaldo Cruz Foundation (Fiocruz), Eusébio, Brazil. ³National Institute of Science and Technology on Neuroimmunomodulation (INCT-NIM), Oswaldo Cruz Institute, Oswaldo Cruz Foundation (Fiocruz), Rio de Janeiro, Brazil. ⁴Department of Clinical and Toxicological Analyses, School of Pharmaceutical Sciences, University of São Paulo, São Paulo, Brazil. ⁵Hospital Israelita Albert Einstein, São Paulo, Brazil. ⁶Department of Neurosciences, Toulouse University Hospitals, Toulouse, France. ⁷Laboratory of Recombinant Technology, Bio-Manguinhos, Oswaldo Cruz Foundation (Fiocruz), Rio de Janeiro, Brazil. ⁸Department of Immunology, Toulouse University Hospitals, Toulouse, France. ⁹Laboratory on Thymus Research (LPT), Oswaldo Cruz Institute (IOC), Oswaldo Cruz Foundation (Fiocruz), Rio de Janeiro, Brazil. ¹⁰Rio de Janeiro Research Network on Neuroinflammation (RENEURIN), Oswaldo Cruz Institute, Oswaldo Cruz Foundation (Fiocruz), Rio de Janeiro, Brazil. ¹¹Department of Dermatology, Medical University of Vienna, Vienna, Austria. ¹²These authors contributed equally: Vinicius Cotta-de-Almeida, Loïc Dupré. ✉e-mail: vinicius.almeida@fiocruz.br; loic.dupre@inserm.fr

This integrin has been particularly studied in the context of multiple sclerosis (MS), in which lymphocytes overexpress VLA-4 on their surface⁷ facilitating transmigration to the central nervous system (CNS)^{8–10}. The identification of this mechanism has been the rationale for targeting VLA-4 as a therapeutic approach to treat MS^{11,12}.

The humanized anti- α 4 monoclonal antibody natalizumab, which blocks VLA-4-VCAM-1 interaction, is currently used to treat relapsing-remitting MS (RRMS) patients^{13,14}. This therapeutic antibody acts primarily by reducing the homing of pathogenic lymphocytes and activated monocytes to the CNS¹⁵. The NEDA endpoint (no evidence of disease activity) is commonly used to define controlled MS¹⁶. Currently, ~35% of MS patients present evidence of disease activity at 2 years¹⁷, such as new or enlarging lesions, relapses or disability progression, not satisfactorily responding to the treatment according to the NEDA criteria. VLA-4 expression on peripheral blood mononuclear cells (PBMCs)¹⁸, serum levels of IgM specific for phosphatidylcholine¹⁹, metalloproteinases²⁰, low percentage of CD5⁺ B cells²¹, age at prescription, and disease duration²² have been pointed as biological parameters related to natalizumab clinical response, although their robustness as predictive biomarkers remain to be established.

To date, a pretreatment test that could predict whether a given person with MS might benefit from the therapy is lacking. This would be particularly relevant to avoid exposing unresponsive patients to potential risks, such as the JC virus-associated progressive multifocal leukoencephalopathy (PML)²³, and to tailor treatment decisions toward other available therapeutic lines. In this context, we reasoned that profiling the in vitro response to natalizumab of leukocytes from MS patients might predict treatment response and therefore assist treatment decisions.

For this purpose, we opted for a high-content cell imaging (HCI) approach to monitor the in vitro effect of natalizumab on PBMCs from persons with MS prior to treatment. This approach allows to extract precise morphological and molecular metrics pertaining to leukocyte adhesion²⁴. Because of its deep phenotyping power, it is also particularly prone to discriminate subtle donor-specific traits that may relate to individual health status²⁵ and responsiveness to therapies²⁶.

Here, we first implement a dedicated HCI approach on healthy donor (HD) PBMCs and MS patient PBMCs to unravel the impact of natalizumab exposure on leukocyte morphology, as well as F-actin and phosphorylated SLP76 levels and distribution. Focusing on CD8⁺ T cells, we then apply unsupervised analysis and build a machine learning-based model to predict natalizumab treatment outcome. Our data highlights the predictive power of the herein developed pre-treatment morphological profiling approach.

Results

High-content cell imaging captures the in vitro sensitivity of primary T cells to natalizumab

Key molecular events underlying the ability of VLA-4 to trigger leukocyte adhesion, spreading and activation are the recruitment of the adapter protein SLP76 and the remodeling of the actin cytoskeleton^{4,27,28}. Therefore, to profile the in vitro response of T cells to natalizumab, we implemented an HCI approach, which offered the possibility to collect concomitantly features pertaining to cell morphology, SLP76 phosphorylation and F-actin organization. The HCI pipeline was first optimized on frozen PBMC samples from ten HD whether exposed in vitro to natalizumab or not and seeded onto VCAM-1-coated 384-well imaging plates for analyzing T-cell subsets based on a staining for the CD4 and CD8 coreceptors. Automated confocal imaging was conducted with a 40X objective by focusing on the basal cellular plane interacting with the VCAM-1-coated surface. It should be noted that our method included the counting of adherent cells and that only adherent cells were considered for the morphological profiling. A set of five descriptors was selected a priori for the analysis, including number of adherent cells, cell area, width-to-length

ratio, phosphorylated SLP76 (pSLP76) and F-actin intensity (Fig. 1A). Natalizumab exposure led to a reduction in cell spreading and in the intensities of the pSLP76 and F-actin stainings in both CD4⁺ and CD8⁺ T-cell subsets (Fig. 1B, C). The combination of the descriptors considered through principal component analysis (PCA) separated the natalizumab-treated from the non-treated samples along component F1 (Fig. 1B, C), indicating a robust effect of natalizumab across the samples. The main descriptors that drove the segregation of treated versus non-treated PBMCs along component F1 were pSLP76 intensity and width-to-length ratio for CD4⁺ cells and cell area for CD8⁺ T cells (Supplementary Table 1). Adhesion on VCAM-1 of both CD4⁺ and CD8⁺ T-cell subsets was severely reduced upon natalizumab exposure in a consistent way across the tested samples (Fig. 1D, E). Natalizumab-induced reduction of cell area was more frequent across the donors in CD8⁺ than CD4⁺ T cells. In contrast, the effects of natalizumab on width-to-length ratio and F-actin intensity were more consistent across the donors in CD4⁺ than CD8⁺ T cells, while pSLP76 intensity was decreased in both T-cell subsets. Combined analysis of cell morphology, F-actin and pSLP76 intensities by automated confocal microscopy is therefore an appropriate approach to capture the sensitivity of T cells to in vitro natalizumab exposure.

CD8⁺ T cells from MS patients are highly sensitive to natalizumab exposure

We next applied the HCI pipeline to PBMC samples from 40 persons with MS who had received at least one first line of treatment but had not yet been treated with natalizumab at the time of sample collection (BIONAT cohort²⁹, see Supplementary Tables 2–8). In addition to CD4⁺ and CD8⁺ T-cell subsets, we extended the evaluation of the in vitro effects of natalizumab to CD14⁺ monocytes and CD19⁺ B cells due to the known contribution of these leukocyte subsets to MS pathogenesis³⁰. Our analysis aimed at defining which subsets within MS PBMCs would be most affected by natalizumab exposure (Fig. 2A). A prominent effect of natalizumab exposure was the global reduction of the spreading of MS PBMCs (Fig. 2B), as observed with the HD T cells. When considering the monocyte subset by gating on the CD14⁺ cells, our method was however not able to clearly distinguish the natalizumab-exposed from the unexposed samples, as shown on the PCA analysis (Fig. 2C). A wide dispersion of the samples was observed when considering CD19⁺ B-cell and CD4⁺ T-cell subsets, with only a partial discrimination of the natalizumab-exposed and unexposed samples (Fig. 2D, E). Such discrimination occurred along the F1 component and was mainly driven by pSLP76 intensity (Supplementary Table 9). The HCI pipeline separated natalizumab-exposed and unexposed samples when considering the CD8⁺ T-cell subset, as shown by the distribution along the F1 component of the PCA plot, mainly driven by cell area and ratio width to length (Fig. 2F and Supplementary Table 9). Therefore, within the tested MS PBMC samples, CD8⁺ T cells appeared to be the most sensitive cell subset to the effects of natalizumab exposure as captured by our image-based approach. By analyzing the effect of natalizumab on the CD8⁺ T cells of the 40 patients, we observed a decrease in the number of adherent cells, in cell spreading and in cell elongation, as well as a modest decrease in pSLP76 intensity (Fig. 2G). As previously observed with the HD PBMCs, F-actin intensity was not reduced in CD8⁺ T cells from MS patients upon natalizumab exposure. These findings demonstrate the robustness of the HCI method to capture the sensitivity of MS patients' PBMCs to natalizumab. Furthermore, it points to CD8⁺ T cells as the cellular subset exhibiting, across patients, the most robust response to in vitro natalizumab exposure.

Unsupervised clustering of HCI data discriminates non-responder MS patients

Based on the reasoning that in vitro natalizumab effects on CD8⁺ T cells prior to treatment might mirror the in vivo treatment efficacy, we next

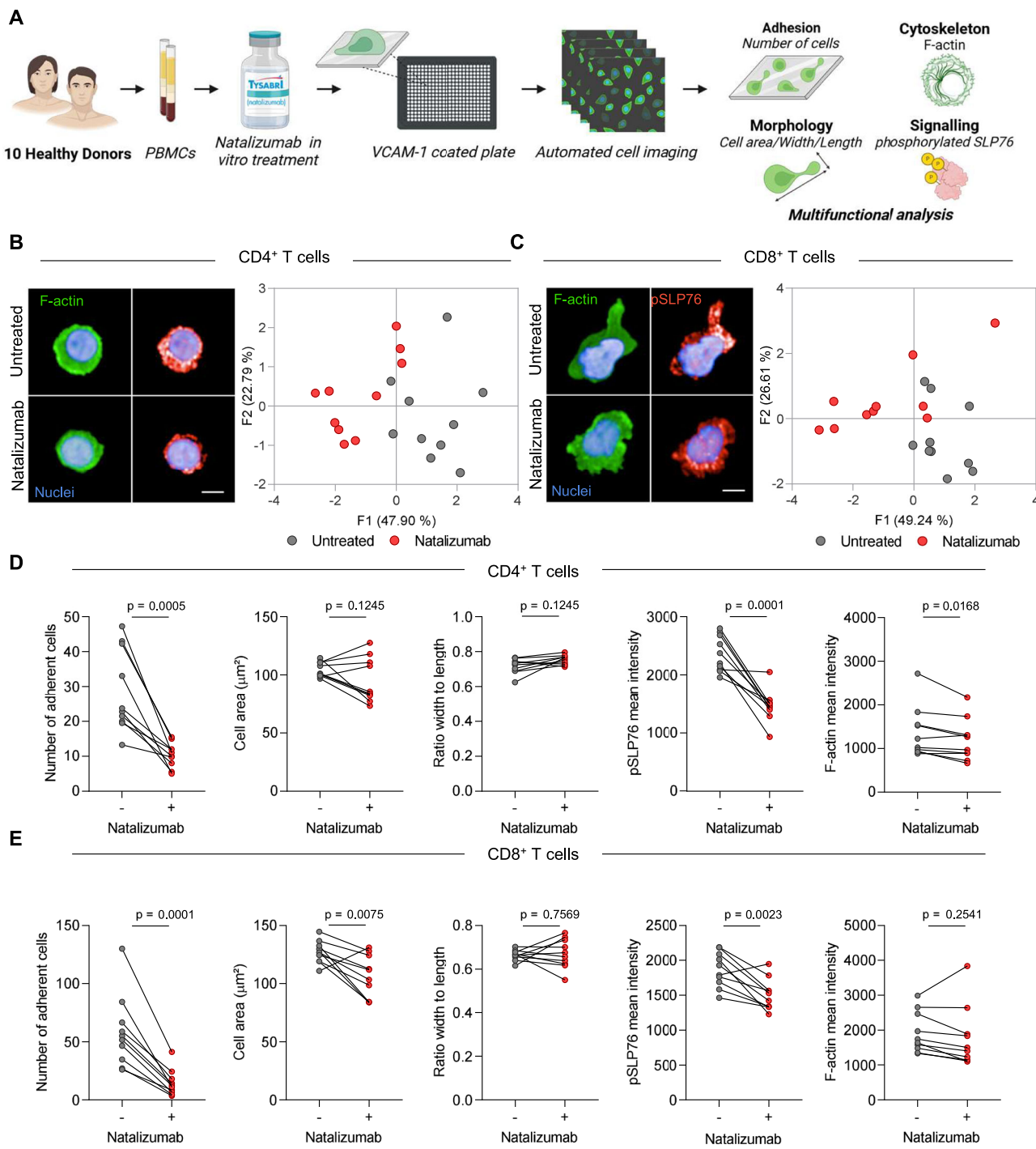


Fig. 1 | Automated cell imaging of healthy donor peripheral blood T cells upon in vitro natalizumab exposure. A Schematic representation of the HCl pipeline applied to PBMCs from healthy donors. PBMCs were exposed or not to natalizumab, seeded on VCAM-1 coated plates, stained for CD4 or CD8, F-actin and pSLP76 and imaged with an automated confocal microscope. Parameters pertaining to cell adhesion, cell shape, F-actin and pSLP76 were extracted separately from CD4⁺ and CD8⁺ subpopulations for further analysis. Created in BioRender. Chaves, B. (2025) <https://BioRender.com/3pcr603>. **B, C** Representative 40x confocal images of CD4⁺ (**B**) and CD8⁺ (**C**) T cells, exposed or not to natalizumab, seeded on VCAM-1 and stained for F-actin (green), pSLP76 (red), and nuclei (blue). Scale bar: 5 μm. PCA plots indicative of the effect of natalizumab on CD4⁺ (**B**) and CD8⁺ (**C**) T cells, based on parameters pertaining to adhesion, morphology, actin and pSLP76 intensity.

D, **E** Values for individual parameters are shown for CD4⁺ T cells (**D**) and CD8⁺ T cells (**E**) in unexposed (gray dots) and natalizumab-exposed (red dots) samples. Parameters include the number of adherent cells, cell area, width-to-length ratio, pSLP76 mean intensity, and F-actin mean intensity. Dots correspond to ten individual donors with data stemming from the mean of two independent experiments, each with two replicate wells. Data were obtained from 20 to 189 CD4⁺ T cells and 14 to 520 CD8⁺ T cells per donor. *p* values were calculated by a two-sided paired *t*-test. Source data for all panels are provided as a Source Data file.

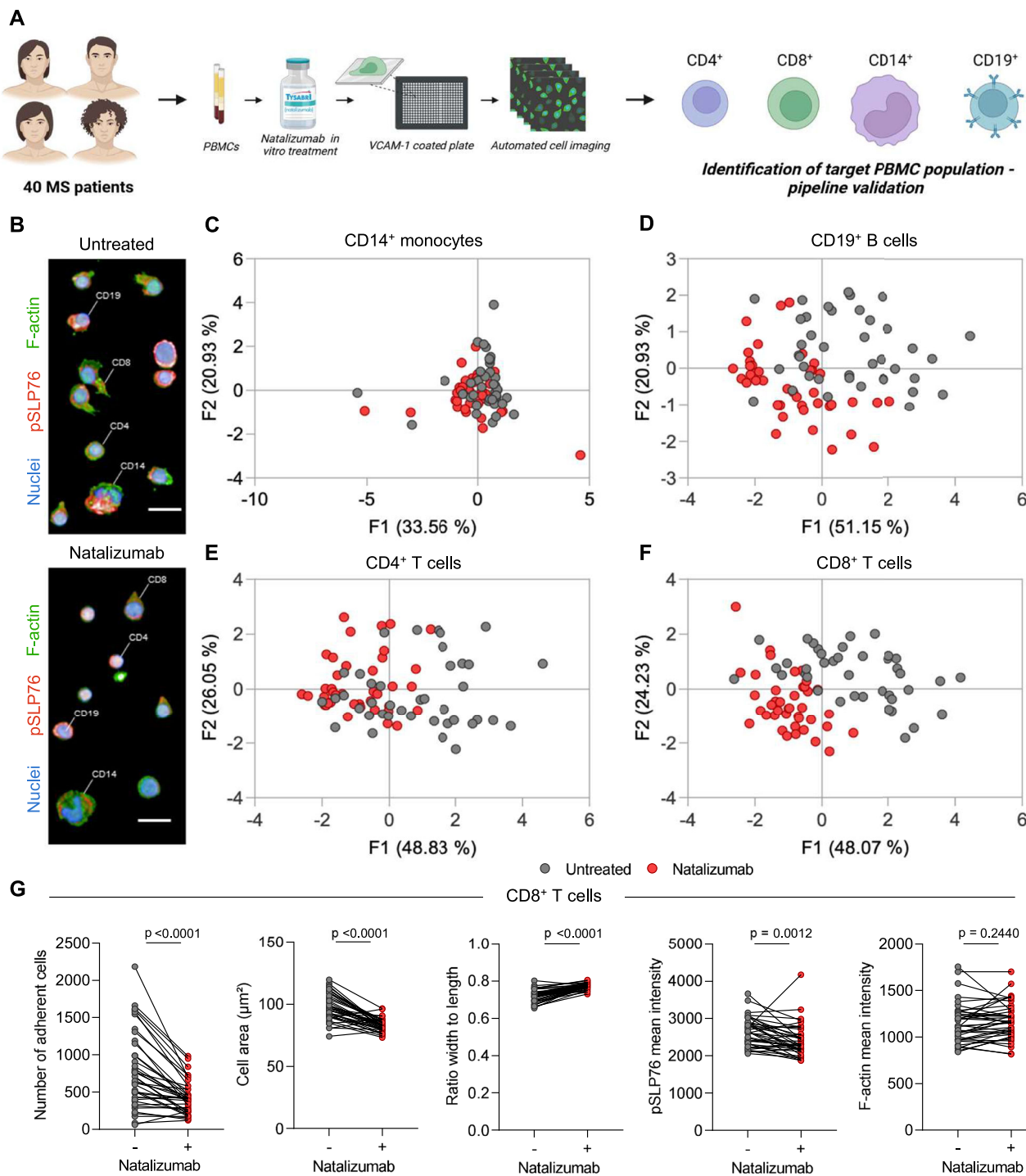


Fig. 2 | CD8⁺ T cells from MS patients display high sensitivity to natalizumab in vitro exposure. **A** Schematic representation of the HCl pipeline applied to pretreatment PBMCs from MS patients. PBMCs were exposed or not to natalizumab, seeded on VCAM-1 coated plates, stained for CD4, CD8, CD14, or CD19, F-actin and pSLP76 and imaged with an automated confocal microscope. Parameters pertaining to cell adhesion, cell shape, F-actin, and pSLP76 were extracted separately from CD4⁺, CD8⁺, CD14⁺, and CD19⁺ subpopulations for further analysis. Created in BioRender. Chaves, B. (2025) <https://BioRender.com/3pcr603>.

B Representative 20x confocal images of PBMCs from a MS patient unexposed (top) or exposed to natalizumab (bottom), seeded on VCAM-1 and stained for F-actin (green), pSLP76 (red) and nuclei (blue). Scale bar: 20 μm . Individual CD4⁺ and CD8⁺ T cells, CD19⁺ B cells and CD14⁺ monocytes are indicated with a white line. Images have been composed from different images to gather representative examples of each cell subset. **C–F** PCA plots indicative of the effect of natalizumab on CD14⁺ monocytes (**C**), CD19⁺ B cells (**D**), CD4⁺ T cells (**E**), and CD8⁺ T cells (**F**)

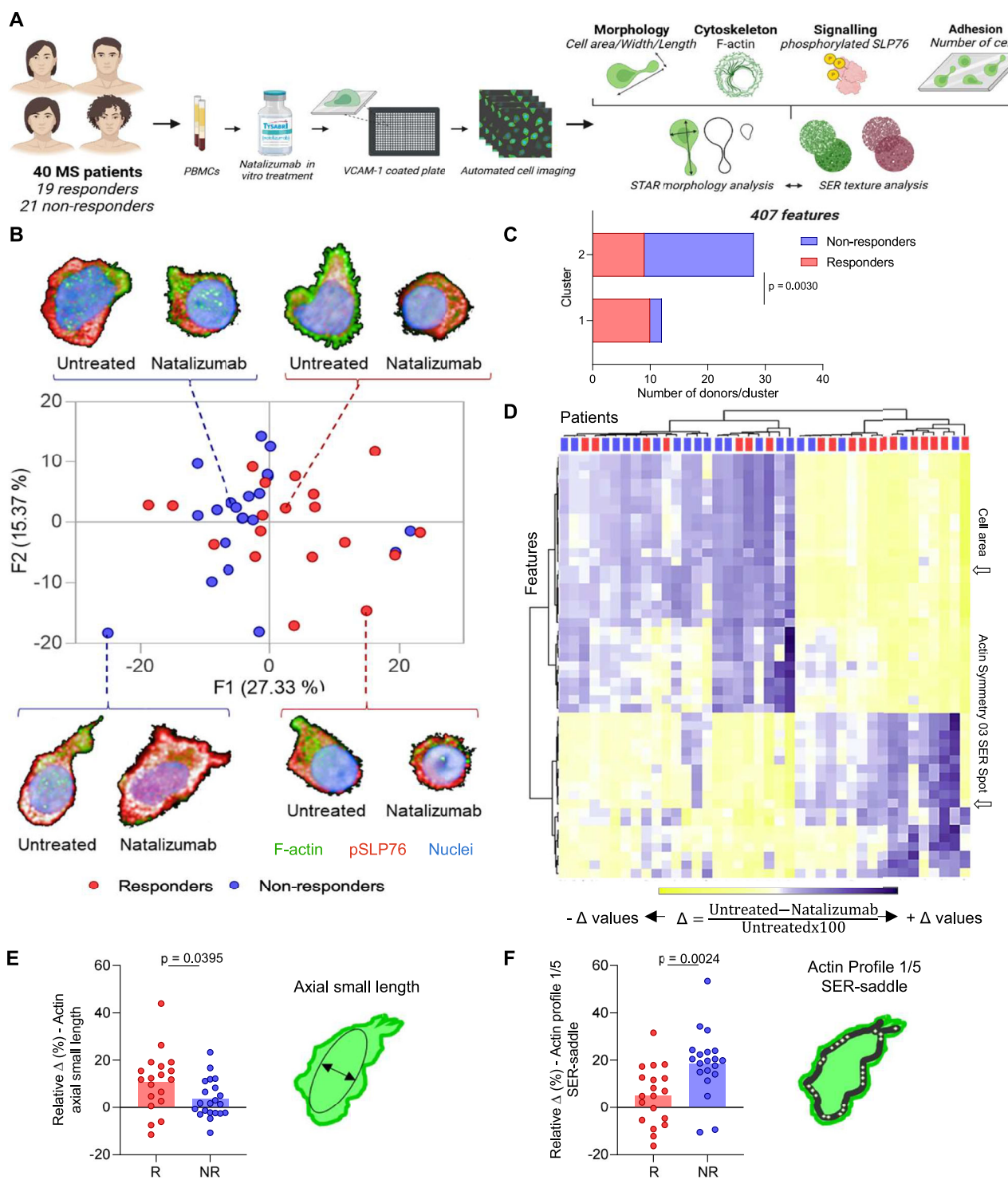
based on parameters pertaining to adhesion, morphology, actin, and pSLP76 intensity. Dots correspond to each of the 40 patients with data stemming from the mean of three independent experiments. Gray dots indicate untreated samples, while red dots represent those treated with natalizumab. Data were obtained from 56 to 9776 CD4⁺ T cells, 22 to 8421 CD8⁺ T cells, 9 to 8050 CD19⁺ B cells, and 3 to 321 CD14⁺ monocytes. **G** Values for individual parameters are shown for CD8⁺ T cells in unexposed (gray dots) and natalizumab-exposed (red dots) samples. Parameters include number of adherent cells, cell area, width to length ratio, pSLP76 mean intensity, and F-actin mean intensity. Dots correspond to each of the 40 patients with data stemming from the mean of three independent experiments. Data were obtained from 56 to 9776 CD4⁺ T cells, 22 to 8421 CD8⁺ T cells, 9 to 8050 CD19⁺ B cells, and 3 to 321 CD14⁺ monocytes. *p* values were calculated by a two-sided paired *t*-test used for statistical evaluation. Source data for all panels are provided as a Source Data file.

tested whether our HCI pipeline could detect differences in PBMC samples obtained before treatment from patients who had responded favorably or not to natalizumab treatment. For that purpose, we selected 40 patients from the BIONAT cohort, corresponding to 19 responders and 21 non-responders to natalizumab therapy, based on the NEDA-3 criteria (Supplementary Tables 2–8). For all selected patients, disease progression was monitored at 2 years after treatment (Supplementary Fig. 1) and the classification into responders or non-responders was based on the decrease of the expanded disability score (EDSS)¹⁶, the number of relapses and the lesion enlargement detected by magnetic resonance imaging (MRI) (Supplementary Fig. 2). The selection of patients from the BIONAT cohort was done by applying a series of successive filters, including availability of NEDA-3 classification after 2 years of treatment, prior treatment washout of at least 1 month, and age/gender pairing of the responder/non-responder subgroups (Supplementary Fig. 3). This first set of 40 patients was denominated discovery cohort. Comparable levels of CD49d were detected at the surface of the different PBMC subsets across the two groups of patients, implying that VLA-4 expression does not by itself determine the response to therapy (Supplementary Fig. 4). PCA analysis of the clinical parameters, demography, blood analysis, and disease progression before treatment initiation (TO) failed to reveal a segregation between responder and non-responder patients (Supplementary Fig. 5A, B and Supplementary Table 10). This motivated the implementation of the HCI pipeline, which was applied to the pre-treatment PBMC samples, focusing on CD8⁺ T cells since they had been identified in the optimization step as the subset most responsive to natalizumab exposure. We increased the sensitivity of the HCI pipeline by imaging the samples with a 63X objective and analyzing an enriched library of 407 preset features (Harmony software) related to the F-actin and pSLP76 stainings and including intensity, morphology (STAR features: cell morphology symmetry, threshold compactness, axial and radial distributions) and texture parameters (SER: spots, edges and ridges). We calculated, for each feature, the difference in absolute value between the natalizumab-exposed and the natalizumab-unexposed samples (mean across cells and wells), which was normalized (referred to thereafter as relative delta) to investigate the effect of natalizumab across multiple features on the same scale (Supplementary Fig. 6). On the basis of these normalized features, an unsupervised PCA analysis was conducted. It partially segregated the samples from the non-responder patients along the F1 component, with 19 of the 21 samples associated with negative F1 values (Fig. 3B). Representative CD8⁺ T cells from responder patients displayed a pronounced reduction of cell spreading and an apparent loss of cell polarity upon natalizumab exposure (Fig. 3B, top right and bottom right). CD8⁺ T cells from a typical non-responder patient displayed reduced spreading upon natalizumab exposure while maintaining a partially polarized shape (Fig. 3B, top left image). CD8⁺ T cells from the most divergent non-responder patient exhibited increased cell width upon natalizumab exposure (Fig. 3B, bottom left image). Samples from responder patients occupied a rather dispersed distribution on the PCA plot. This analysis suggests that CD8⁺ T cells from the non-responder patients were less sensitive to in vitro natalizumab exposure in terms of cell morphology alterations. The segregation between responder and non-responder patients was not apparent anymore when the PCA analysis was applied to the separate sets of data corresponding to the untreated and natalizumab-exposed samples (Supplementary Fig. 7), indicating that morphological profiling at baseline is not sufficient to distinguish response groups and highlighting the importance of normalizing the effect of natalizumab-exposure on the basis of the basal states of the samples. The impact of natalizumab on cell adhesion was also considered as a potential discriminating parameter. However the reduction in adherent numbers of CD8⁺ T cells upon natalizumab exposure was identical among the two treatment response groups (Supplementary Fig. 8). The discrimination of non-responder samples

was further confirmed by a complementary unsupervised K-means clustering analysis built from the 407 features that identified two clusters, including one that gathered 19 of the 21 samples from the non-responder patients (Fig. 3C). We further applied a Ward clustering approach, built with the 50 most important features from the PCA (Supplementary Table 11). It segregated the samples into two main branches, with the left one gathering 16 of the 21 samples from the non-responder patients (Fig. 3D). This branch comprised a majority of features whose values were poorly impacted by natalizumab exposure, as opposed to the right branch composed mainly by responder samples. These features included axial small length, cell and nucleus area, cell width and multiple F-actin, and pSLP76 texture-related descriptors (Fig. 3D and Supplementary Table 11). On the other hand, a minority of discriminative features had values that were highly reduced by natalizumab exposure in the non-responder branch, such as Actin symmetry O3 SER-spot, that can be interpreted as actin dots uniformly distributed in three parts of the considered cells. Analysis of actin axial small length (Fig. 3E), and actin profile 1/5 SER-saddles (Fig. 3F) indicated that non-responders were less sensitive to the impact of natalizumab on morphology but tended to lose actin structures towards the cell periphery. Together, this unsupervised morphological analysis indicates that CD8⁺ T cells from non-responder patients display reduced loss of cell spreading and polarity upon in vitro exposure to natalizumab.

Prediction of natalizumab treatment outcome with a machine learning model

As the unsupervised analysis indicated a partial discrimination of responder and non-responder patients based on how natalizumab impacted CD8⁺ T-cell features, we implemented a machine learning approach to investigate whether samples from responder and non-responder patients could be distinguished. We opted for a random forest (RF)-based approach that trained individual models with the features from the image dataset generated from the 40 MS patient samples, labeled as the discovery cohort (Fig. 4A). Our goal was to robustly predict natalizumab treatment response through the extracted morphological features. To enhance performance and reduce redundancy, features with >90% correlation were removed, refining the feature set to 133 out of the initial 407 features. Based on the 20 most important features selected by the RF approach, we trained models using 1,048,575 feature combinations. The F1 score was chosen as the main performance parameter to evaluate the prediction power. This score represents a harmonic mean of precision and sensitivity, which helps maximizing correct response classifications while minimizing overall sample misclassification (Fig. 4B). The RF approach allowed us to identify combinations that distinguished responder from non-responder patients, achieving a F1 score of 92.3% and comparable scores for the other tested performance metrics (Fig. 4C). Among the 20 most important features used for prediction, 13 were related to actin segmentation, symmetry and texture, five to pSLP76 distribution symmetry and texture, and two to cell morphology (Fig. 4D). Beyond the importance of each feature, we looked at their frequency in combination trees with performance above 85%. Certain features with relatively low RF importance, such as actin symmetry O5 SER-saddle, nevertheless appeared much more frequently than others with higher importance (Fig. 4D). The discrepancy between importance and frequency highlights the relevance of taking both parameters into account and analyzing different feature combinations to identify the most relevant features for prediction, for example, Actin profile 3/5 SER-bright and 1/5 SER-dark present, on this prediction set, high importance and frequency. To challenge the robustness of the HCI approach to predict treatment response, it was applied to a validation cohort, composed of 14 responders and 13 non-responder patients. We tested the same 1,048,575 combinations of features to evaluate their performance on the validation cohort using the 20 most important



features as identified through the analysis of the discovery cohort. The most accurate combinations were associated with a performance of 88.8% (Fig. 4E). Although comparable performance was achieved for the two cohorts, the most important features for prediction and their frequency of occurrence in combinations were different across the two cohorts (Fig. 4D, F). Actin profile 3/5 SER-bright, for example, had a decrease in the importance rank. When comparing the predictive performance of the two cohorts, we identified three combinations (Supplementary Table 12) from a set of seven features (Fig. 4F, arrows) that consistently appeared in models with performance above 85%. This highlights the robustness of our approach in predicting treatment response at the individual patient level through HCl-extracted

parameters. We also considered that first- and second-line treatment received by the patients, as well as washout duration prior to sampling, might have affected our analysis. Although the immunomodulatory treatment seemed to impact key baseline features in CD8⁺ T cells, we could verify that it did not act as a confounding factor in our analysis (Supplementary Note 1 and Supplementary Fig. 9A-C). To further examine how the selected features (Supplementary Fig. 10) discriminated patient groups, we combined the cohorts and applied a *t*-test with Bonferroni correction. Three actin-related features were impacted by natalizumab specifically in CD8⁺ T cells from non-responders (Fig. 4G-I), including Actin profile 2/5 SER-edge, which belonged to the set of 7 most consistent features (Fig. 4G). On the

Fig. 3 | Automated cell imaging discriminates CD8⁺ T cells according to natalizumab treatment outcome in MS patients. **A** Schematic representation of the HCI pipeline applied to pretreatment PBMCs from MS patients and aiming at identifying morphological signatures associated with natalizumab treatment outcome. PBMCs were exposed or not to natalizumab, seeded on VCAM-1 coated plates, stained for CD8, F-actin, and pSLP76 and imaged at high resolution with an automated confocal microscope. A total of 407 parameters were extracted from each imaged CD8⁺ T cell for further analysis. Created in BioRender. Chaves, B. (2025) <https://BioRender.com/3068pk0>. **B** Representative 63x confocal images of CD8⁺ T cells from four MS patients exposed or not to natalizumab, seeded on VCAM-1 and stained for F-actin (green), pSLP76 (red), and nuclei (blue). Scale bar (brackets): 45 μm. PCA plot aggregating the data from 407 features pertaining to cell adhesion, morphology, F-actin and pSLP76 intensity, distribution and texture (Harmony STAR morphology and SER texture features). Each feature was analyzed as a normalized delta value ((unexposed sample – natalizumab-exposed sample)/natalizumab-exposed × 100) to account for the effect of natalizumab. Each dot represents a single MS patient with data stemming from the mean of three independent experiments. Clinical response to natalizumab treatment is indicated by the dot color: red dots indicate responders, while blue dots represent non-

responders. Data were obtained from four to 1598 CD8⁺ T cells. **C** K-means clustering analysis of the entire HCI dataset, yielding two clusters that partially segregated responder (red) or non-responder patients (blue). *p* values were calculated by a two-sided χ^2 test. **D** Ward clustering analysis of the HCI dataset represented as a heatmap with a dendrogram. The analysis was restricted to the 50 top features along the F1 component of the PCA. The upper dendrogram represents the clustering of the 40 patients, indicating partial segregation of responder (red) or non-responder patients (blue). The left dendrogram represents the clustering of the 50 features, according to the intensity and the direction of the effect of natalizumab exposure (dark purple: natalizumab exposure increases the value of the considered feature; yellow: natalizumab exposure reduces the value of the considered feature). **E, F** Relative delta values are shown for actin axial small length (**E**) and actin profile 1/5 SER-saddle (**F**), two features exemplifying the distinct in vitro effect of natalizumab on CD8⁺ T cells from responder (R, red dots) and non-responder patients (NR, blue dots). Bars represent the mean of the considered patient subgroup. Data were obtained from 4 to 1598 CD8⁺ T cells. *p* values were calculated by a two-sided unpaired *t*-test with Welch's correction. Schematics of the actin axial small length and actin profile 1/5 SER-saddle are represented on the side of the corresponding graphs. Source data for all panels are provided as a Source Data file.

other hand, CD8⁺ T cells from responders displayed greater sensitivity to natalizumab-induced changes in cell spreading, as indicated by changes in nucleus area and cell area (Fig. 4J, K). Although natalizumab-mediated differences in actin distribution were observed among the two patient groups, F-actin intensity levels are similar between responder and non-responder CD8⁺ T cells (Supplementary Fig. 11). The combination of our HCI-based analysis with a supervised model therefore suggests that patient-specific responses to natalizumab of the BIONAT cohort can be captured in vitro prior to treatment in a way to predict the in vivo treatment response.

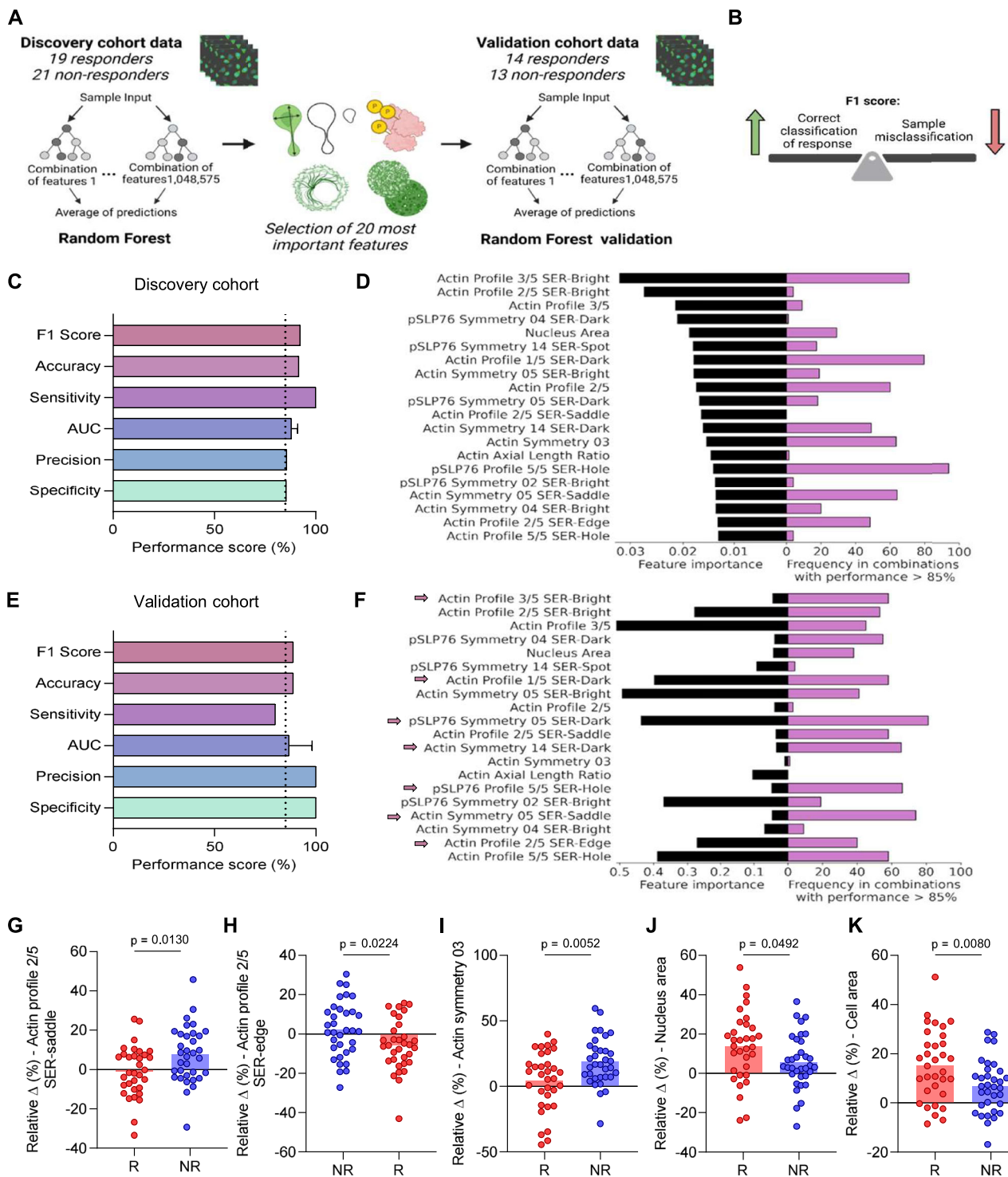
CD8⁺ T cells from non-responder patients tend to resist the impact of VLA-4 blockade on morphology through an actin polymerization-dependent mechanism

To gain insight into the biological underpinnings of the diverging therapeutic responses, we next asked how the morphological and actin remodeling effects of natalizumab on CD8⁺ T cells from responder and non-responder patients may translate into their ability to migrate over VCAM-1. Given the apparent milder impact of natalizumab on the spreading of T cells from non-responder patients, we tested whether they would be more prone to maintain an elongated shape and would display a migratory advantage over T cells from responder patients. For that purpose, we expanded CD8⁺ T cells from 4 representative non-responder and responder samples (Supplementary Fig. 12A), which were paired in VCAM-1-driven migration assays in an under-agarose setting. This assay imposes a confined environment, as a way to mimic conditions encountered in vivo, and allows to compare cell morphology, velocity, and straightness (Fig. 5A). T cells tended to form homotypic aggregates upon natalizumab exposure (Fig. 5B, right), as previously reported for other anti-VLA-4 antibodies³⁰, but this phenomenon appeared to impact comparably CD8⁺ T cells from both patient groups (Fig. 5C). Analysis of cell area confirmed that CD8⁺ T cells from non-responder patients were relatively resistant to the reduction of cell spreading evoked by natalizumab (Fig. 5D). Interestingly, tracking analysis indicated that intrinsic velocity and ability to migrate along straight paths, rather than response to natalizumab per se, were the parameters that distinguished CD8⁺ T cells from the considered responder and non-responder patients (Fig. 5E, F). This complementary live microscopy assay therefore suggests that intrinsic differences in the propensity to migrate over VCAM-1 might differentially predispose CD8⁺ T cells to the activity of natalizumab. To further investigate whether these migration behaviors might be related to distinct actin remodeling responses, we selected T cells from two representative patients per group, exposed the cells to natalizumab, as well as to the actin inhibitors latrunculin B (LAT, blocking actin polymerization) or jasplakinolide (JASP, inhibiting actin depolymerization).

The cells were seeded on VCAM-1 and stained for F-actin, α-tubulin and the ARP2/3 subunit ARPC1B, which governs actin branching. To globally assess the effects of the drugs on morphology, PCA aggregating 251 features related to F-actin, α-tubulin, and ARPC1B were constructed (Supplementary Fig. 12B). LAT appeared to have a more pronounced effect than JASP. To refine this analysis, the effects of the drugs were further evaluated at a single cell level (Supplementary Fig. 12C). Interestingly, cells from responder and non-responder patients partially segregated but such segregation was lost upon LAT treatment, implying that integrity in actin polymerization during the HCI assay was important to reveal the patient subgroup. LAT treatment appeared to prevent the propensity of natalizumab to induce cell rounding, as measured by the ratio of width to length (Fig. 5G). Interestingly, the non-responder cells, which tend to maintain a more elongated shape than the responder cells (as also seen in Fig. 3E), were less affected by the LAT treatment. ARPC1B distribution was more polarized in non-responder cells (Fig. 5H), and this polarization appeared to vanish upon LAT treatment. These observations suggest that ARPC1B-dependent actin branching supporting leading edge assembly might be maintained in non-responder cells, endowing them with a migratory advantage. Collectively, our analysis suggests CD8⁺ T cells from non-responder patients adopt a distinct actin remodeling response upon natalizumab exposure, which is associated with the maintenance of spreading and migration processes.

Discussion

Although natalizumab has revolutionized the treatment of relapsing-remitting MS, a substantial proportion of treated patients experience disease relapse. The incomplete response rate (35%) to natalizumab treatment at one year, and even more thereafter¹⁷, carries a high societal and human burden to health institutions and to the patients and their families. In this context, strategies to predict natalizumab efficacy would allow for the implementation of personalized treatment schemes. Multiple parameters have been proposed to account for treatment failure in individual patients. Given the multiplicity of cellular subsets expressing α4 integrin subunit and the multiplicity of cellular activities that VLA-4 blockade through natalizumab may alter, identifying a biomarker to discriminate and eventually predict individual patient response has remained challenging. Herein, we designed a high-content image-based approach applied to human PBMCs to monitor, through multiple morphological and molecular parameters, the sensitivity of patient cells to natalizumab upon ex vivo exposure. We further tested whether such ex vivo challenge would capture inter-individual variability that might align with the clinical outcomes of individual MS patients treated with natalizumab.



In the context of personalized medicine, HCl is emerging as a unique approach that simultaneously captures molecular information and cellular morphometrics with single-cell resolution. The application of HCl in drug testing workflows might generate results within a few days³¹ and deliver treatment efficacy prediction with high prediction accuracy³². The potential of HCl to provide support for treatment decision has recently been highlighted by its ability to predict drug efficacy in patients with hematological cancers^{26,33}. Here, we took the challenge of testing whether HCl might be applicable to screen the efficacy of a therapeutic antibody on non-neoplastic immune cells in the context of an auto-immune disease. Different from previous HCl studies that monitored tumor cell viability and global activity of

surrounding immune cells, our approach was tailored to assess the specific activity of the VLA-4-targeting antibody natalizumab, by stimulating PBMC from persons with MS on VCAM-1 and exposing them to natalizumab. We opted for high-resolution confocal acquisition, aiming to precisely capture multiple cell morphological features, as well as parameters related to F-actin organization and SLP76 distribution, given the central position of these molecular activities in the response of leukocytes to VLA-4 engagement.

We provide evidence that such an approach focused on the mechanism of action of natalizumab presents several advantages compared to what has been achieved so far in terms of natalizumab response prediction: timing of prediction, cohort size, statistical

Fig. 4 | Random forest approach predicts natalizumab treatment outcome in MS patients. A schematic representation of the machine learning approach built to predict response to natalizumab treatment based on the analysis of pretreatment PBMCs with the HCl pipeline. A random forest (RF) model was trained on the HCl dataset from a discovery cohort composed of 19 responders and 21 non-responder patients. The elaborated model, which runs with 1,048,575 combinations of a restricted set of 20 features, was then challenged with the HCl dataset from a validation cohort composed of 14 responders and 13 non-responder patients. Created in BioRender. Chaves, B. (2025) <https://BioRender.com/3068pko>.

B Schematic drawing of the F1 score parameter, which maximizes the performance of correct response classification and limits incorrect classification of patients. Created in BioRender. Chaves, B. (2025) <https://BioRender.com/mx3ulna>.

C, E Parameters of RF performance evaluation of discovery (C) and validation (E) cohorts. Prediction was performed with the 20 most important features pointed out by the RF. All possible combinations of these features were tested, yielding 1,048,575 combinations. Parameters are shown for combinations that achieved an

F1 score of $\geq 85\%$ in both cohorts, to ensure robustness. Data were obtained from 8 to 6285 CD8⁺ T cells and calculated on the normalized delta values. The dashed line depicts a threshold of 85% above which the parameters are associated with high performance. **D, F** Feature importances (black) and frequencies on RF combinations with F1 score $\geq 85\%$ (pink) for the discovery (**D**) and validation (**F**) cohorts. Arrows point to common features on RF combinations with an F1 score $\geq 85\%$ across the two cohorts. **G–K** Relative delta values are shown for actin profile 2/5 SER-saddle and SER-edge (**G, H**), actin symmetry O3 (**I**), nucleus area (**J**), and cell area (**K**). The relative delta values represent the in vitro effect of natalizumab on CD8⁺ T cells from responder (R, red dots) and non-responder patients (NR, blue dots). Data were obtained from CD8⁺ T cells from 67 MS patients, corresponding to 8 to 6285 CD8⁺ T cells per condition. Data stems from the mean of three independent experiments per patient. Bars represent the mean of the considered patient subgroup. p values were calculated by a two-sided unpaired t-test with Bonferroni correction (significance = $p \leq 0.0025$). Source data for all panels are provided as a Source Data file.

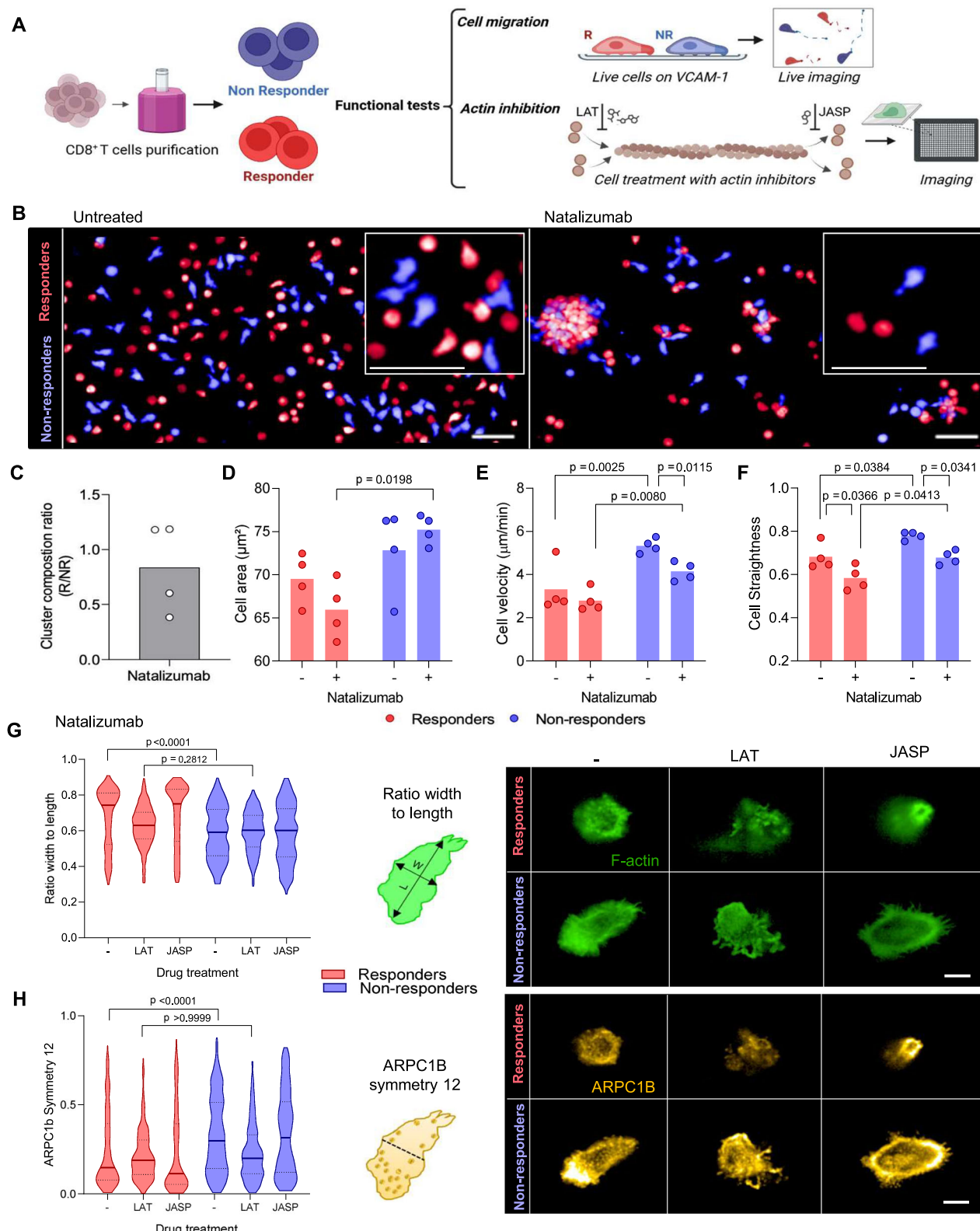
strength and biological explanation. Several studies have aimed at predicting the efficacy of natalizumab treatment. High anti-phosphatidylcholine IgM levels in the serum were associated with treatment response in a study involving 33 patients¹⁹. In our study, IgM titers did not diverge among the responder and non-responder patients (Supplementary Fig. 5B), although specific quantification of IgM to phosphatidylcholine was not performed. Decreased levels of B cells and intrathecal immunoglobulin synthesis in the cerebrospinal fluid were also associated with optimal response through the evaluation of 23 patients under treatment²¹. Another study involving 30 patients under natalizumab treatment pointed to a decrease in metalloproteinases serum levels in patients with no relapse episodes²⁰. Two studies performed with 29 and 49 patients under treatment pointed to CD49d expression in leukocytes as a biomarker for determining optimal dose and predicting treatment efficacy^{18,34}. Our analysis conducted on PBMC samples prior to treatment, however, failed to establish a link between CD49d expression and natalizumab treatment efficacy, potentially reflecting that the profile of CD49d expression might be altered during the treatment. Initiation of treatment at a maximum of 37.5 years of age and 9.5 years of disease duration were identified as parameters of optimal response to natalizumab therapy in a study of 48 patients²². In our set of 67 selected patients, age and disease duration were equivalent between the two groups of patients to avoid their confounding effect (Supplementary Figs. 13A, 14A). Interestingly, we observed a mild correlation of some HCl features with age and disease duration within the non-responder subgroup (Supplementary Figs. 13B, 14B), suggesting that our model may capture some age-related subtleties in non-responders, and this observation might contribute to the prediction performance. Those previous studies of natalizumab efficacy prediction were conducted with classical statistical analysis by evaluating the fitness of individual biological or patient-related parameters. They suffered from not evaluating the robustness of the considered parameters in independent cohorts. Most of them were conducted during treatment and did not evaluate the predictive value of the considered parameters before treatment initiation. In this context, our approach proposes a paradigmatic shift in the search for a treatment efficacy predictor. By combining a miniaturized and automatized image-based bioassay and machine learning approaches, we extract individual patient signatures directly reflecting the quantitative and qualitative impact of natalizumab on primary cells from the patients. It presents predictive values of accuracy and F1 score above those of previous studies that applied machine learning methods to predict clinical outcome in other disease settings^{35,36}. We anticipate that our workflow could be generalized to the testing of other therapeutic antibodies across multiple clinical indications.

The HCl pipeline identified CD8⁺ T cells as a relevant subpopulation to predict response to natalizumab. Alterations in the metabolic and inflammatory profile of CD8⁺ T cells play an important role in MS

development by enhancing their activation and migration toward the CNS³⁷. In addition, the CD8⁺ T-cell subset was previously suggested as a cell population to predict PML development risk in MS patients³⁸. These findings underscore the importance of studying CD8⁺ T cells to gain deeper insights into MS progression, develop new therapies, and guide treatment selection. We failed to detect substantial effects of natalizumab exposure on monocytes. This finding might agree with the natalizumab-induced upregulation of $\alpha 4$ on monocytes³⁹, contrasting with the downregulation of $\alpha 4$ on lymphocytes¹⁸. Despite the VLA-4 mediated role of B cells in MS neuroinflammation⁴⁰ and the role of natalizumab targeting this population our study did not succeed using B cells population to determine natalizumab effect and predict patient response. Possibly, an adaptation of the HCl pipeline, such as increasing the time of adhesion, can be performed to reveal a clear impact of natalizumab on this cell population.

The prediction of natalizumab patient clinical outcome by machine learning was mainly driven by a set of actin-related features associated with how CD8⁺ T cells adhere, enrich, and distribute actin at the adhesion plane, spread and elongate on VCAM-1. The role of integrins in promoting cell spreading and their implication in many diseases are well established^{41–43}. The HCl pipeline leads to the identification that non-responder patients are resistant to natalizumab-induced decrease on cell spreading and elongation, which are morphological adaptations needed to allow T-cell interstitial migration and formation of motility related structures such as the lamellipodia and the uropod⁴⁴. Our data point to an increased migratory profile of the CD8⁺ T cells from the non-responder patients. Thus, we hypothesize that by preserving cell spreading ability, non-responder CD8⁺ T cells have an increased capacity to transmigrate towards the CNS and to establish an immune synapse with target cells, leading to cell killing and consequent inflammation in the CNS. VLA-4 is essential for forming adhesive structures through actin polymerization⁴⁵. Upon natalizumab treatment, responder cells become rounder with less ARPC1B at the leading edge, but blocking actin polymerization shifts them to a non-responder profile. We hypothesize that VLA-4 antagonism drives actin polymerization to maintain cell shape and prevent polarization, though further studies are needed to confirm this mechanism.

Despite the potential of our analysis in coupling HCl of patient PBMCs to machine learning algorithms and providing biological interpretation, validation in larger cohorts across multiple clinical centers would be necessary before translation in medical practice. In this study, we have not investigated whether a more precise examination of the effects of natalizumab on T-cell subsets relevant for the immunopathology of MS might have revealed selective effects. We here considered a predefined library of features, and mean values across all imaged cells were extracted. It is expected that a full exploitation of the data at the single-cell level, combined with unsupervised image analysis based on convolutional neural networks⁴⁶,



would be even more powerful at segregating response groups and identifying underlying mechanisms. We have also not tested whether our pipeline might predict the risk of developing serious side effects such as PML. To reinforce the relevance of the HCl approach, it will be interesting to study how the distinct morphological and actin remodeling effects of natalizumab on CD8⁺ T cells from responder and non-responder patients may be sustained by distinct molecular responses and translate into distinct motility capacities.

Our study shows how HCl combined with machine learning algorithms may serve as a treatment testing platform to guide treatment prescription. The less sophisticated measurement of a single key biological marker might sound like a more desirable approach. However, our study clearly indicates that among many considered parameters, none could by itself be discriminative enough to predict treatment outcome. Since automated high-content cell imagers are becoming increasingly available in the technological portfolio of

Fig. 5 | CD8⁺ T cells from non-responder patients are resistant to natalizumab inhibition of cell spreading in an actin polymerization-dependent manner.

A Schematic representation of the functional tests used to assess the differences between responder and non-responder patients. CD8⁺ T cells from responder and non-responder patients were purified and submitted to two distinct functional tests: under-agarose migration and exposure to F-actin inhibitory drugs. Created in BioRender. Chaves, B. (2025) <https://BioRender.com/56lb3fy>. B Representative snapshots of migrating CD8⁺ T cells from one responder and one non-responder MS patient under-agarose in the presence of VCAM-1. Blue indicates non-responder cells, and red indicates responder cells. Scale bars represent 40 μm. To the right of each image, a representative zoom of cells exposed or not to natalizumab. C Ratio of responder/non-responder cells per homotypic aggregation cluster. Bar represents the average of four responder cells and four non-responder cells exposed to natalizumab after 1 h of migration. Data stems from the mean of two independent experiments per donor. D–F Cell area, cell velocity, and cell straightness of CD8⁺ T cells from four responders and four non-responder MS patients migrating under-agarose in the presence of VCAM-1. Data were obtained from 816 to 1417 CD8⁺

T cells per patient. Bars represent mean values along 2 h of migration. Clinical response to natalizumab treatment is indicated by colors: red dots and bars indicate responders, while blue represents non-responders. Data stems from the mean of two independent experiments. *p* values were calculated by a Tukey's multiple comparisons test. G, H Width to length ratio (G) and ARPC1B symmetry 12 (F) features of CD8⁺ T cells from two responder and two non-responder MS patients exposed to natalizumab, stimulated on VCAM-1 and treated with the actin drugs latrunculin B (LAT) or jasplakinolide (JASP) for 10 min where indicated and stained for F-actin (green) and ARPC1B (gold). Red violin plots indicate responders, while blue represents non-responders. Data were obtained from 16 to 1067 cells per condition with two replicate wells. Full lines represent median values, dashed lines represent upper and lower quartiles. *p* values were calculated by a Dunn's multiple comparisons test of responder and non-responder samples in the conditions without drug and LAT. Schematic drawings of cell ratio, width to length and ARPC1B symmetry 12 are represented on the side of each corresponding graph. Confocal images were acquired with a 63x objective. Scale bar: 5 μm. Source data for all panels are provided as a Source Data file.

biomedical research centers, the development of standardized bioassays based on this technology might become feasible in the near future.

Methods

Cells from healthy donors and persons with MS

PBMCs from healthy donors (HD). Frozen PBMCs from HD were obtained from the Etablissement Français du Sang. The study design and conduct of this study complied with all relevant regulations regarding the use of human study participants and was conducted in accordance with the criteria set by the Declaration of Helsinki and as per French Bioethics law. Sex and age of the HD are stated in Supplementary Table 13. The study on the PBMCs from HD was approved by the French South-West & Overseas ethical committee and was registered at the French Ministry of Higher Education and Research (DC-2015-2488). PBMCs were thawed in RPMI-based growth medium (RPMI media (Gibco), 5% human serum (heat inactivated, AB positive blood type, Institut de Biotechnologies Jacques Boy), 100 U/ml penicillin/streptomycin (Gibco), 1 mM sodium pyruvate (Gibco), 1X MEM non-essential amino acids (Sigma), 10 mM HEPES (Gibco). Cells were maintained for 16 h at 37 °C and 5% CO₂ before being processed through the HCI workflow. Cellular composition was analyzed by measuring CD3, CD49d, CD4, and CD8 expression by flow cytometry.

PBMCs from persons with MS. Frozen PBMCs from 68 MS patients were obtained from the BIONAT cohort²⁹. The study design and conduct of this study complied with all relevant regulations regarding the use of human study participants and was conducted in accordance with the criteria set by the Declaration of Helsinki and as per French Bioethics law. All recruited volunteers provided written informed consent. This research received a favorable opinion from the Committee for the Protection of Persons (CPP) Sud Ouest et Outre Mer II on 06/02/2009, received authorization from the competent authority on 09/02/2009, and was declared to the Commission Nationale Informatique et Libertés (CNIL). The registration number at ClinicalTrials.gov is NCT00942214. Samples included in this study were obtained from relapsing-remitting MS patients aged 18 to 63 years. Out of the 67 patient samples, 20 were from male individuals and 47 from female individuals. This study is not sex-centered, however, it is important to remark that the majority of MS patients included are female due to the MS prevalence of more than 70% in female individuals⁴⁷. The herein studied blood samples were collected prior to natalizumab treatment, from which PBMCs were prepared and frozen. Samples were thawed in complete RPMI medium (as HD samples) and maintained for 16 h at 37 °C and 5% CO₂ before being processed through the HCI workflow. Details for each patient are available in

Supplementary Tables 2–8. Cellular composition was analyzed by measuring CD3, CD49d, CD4, and CD8 expression by flow cytometry.

CD8⁺ T cells from MS patients. When applicable, PBMCs leftovers were kept in culture for 5 days in complete medium and supplemented with IL-2 100 IU/mL and PHA 2 μg/mL. CD8⁺ T cells were then purified using a CD8⁺ T-Cell Isolation Kit (Miltenyi Biotec) and following the manufacturer's instructions.

NEDA-3 classification

Classification into responder or non-responder patients was performed according to the NEDA-3 score⁴⁸. No evidence of disease activity-3 is calculated based on the absence of clinical relapses, confirmed disability progression, and new or enlarging lesions on brain magnetic resonance imaging. If a person with MS under treatment has experienced no clinical relapse, no confirmed disability worsening and no new lesions during 2 years, he/she is considered a responder to natalizumab therapy.

High-content cell imaging of PBMCs from HD

The description of all antibodies, recombinant proteins, chemicals, buffers, equipment, and software are available in Supplementary Tables 14–16.

Staining. High-content screening 384-well imaging plates (CellCarrier-384 Ultra, Perkin Elmer) were coated overnight at 4 °C with VCAM-1 (R&D Systems) at 0.625 μg/mL. The coated wells were washed with phosphate-buffered saline (PBS) and cell culture medium. PBMCs from HD (thawed the day before) were centrifuged at 430 × g for 5 min, counted and treated or not with natalizumab (Biogen) or a Human IgG4 isotype control (Biolegend) at the final concentration of 2 μg/mL. Cells were incubated for 30 min at 37 °C and 5% CO₂. Next, cells were washed to remove excess antibody. A total of 9000 cells/30 μL were seeded per well of the 384-well precoated plates, followed by a 10 s centrifugation. After stimulation for 10 min at 37 °C, non-adherent cells were removed by flipping the plates. Subsequently, cells were fixed using 3% paraformaldehyde (PFA), washed with PBS and permeabilization buffer (PB, eBioscience), and then stained with 1:500 Alexa Fluor™ 488 Phalloidin (Thermo Fisher), 1:500 anti-pSLP76 antibody and 1:500 anti-CD4 or anti-CD8 antibodies (R&D systems). After incubation overnight at 4 °C, plates were washed with permeabilization buffer and stained with 1:200 anti-rabbit Alexa 647 (Thermo Fisher), 1:200 anti-mouse IgG2a Alexa 546 antibodies and 1:1000 4',6-diamidino-2-phenylindole, dihydrochloride (DAPI, Thermo Fisher). After 1 h incubation, plates were washed three times with PBS and subjected to automated confocal imaging. The specificity of natalizumab in blocking VCAM-1 evoked cell adhesion was assessed by

comparing the number of adherent cells that had been left unexposed or had been exposed to natalizumab or the isotype control. Given that the isotype did not impact cell adhesion when compared to the unexposed condition (analysis focused on CD8⁺ T cells, see Supplementary Fig. 15A), the HCI runs were performed with the unexposed versus natalizumab-exposed conditions. We also verified that natalizumab impacted the adhesion of purified CD8⁺ T cells, pointing to a direct effect of natalizumab on these cells rather than an indirect effect via other cell subsets present in the PBMC samples (Supplementary Fig. 15B).

Image acquisition. Images were acquired with a high-content screening system (Opera Phenix, Perkin Elmer) equipped with a 40 × 1.1 NA Plan Apochromat water immersion objective, 4 sCMOS cameras (2160 × 2160 pixels, 16 bits, 6.5-μm pixel) and a Yokogawa spinning disk confocal unit. For each well, 49 fields-of-view and four Z-planes per field (with a step of 0.5 μm, starting at the cell contact plane with the substrate) were acquired. Z-stacks of images were projected along the Z-axis using maximum intensity global projection and flatfield correction using Harmony software. Z-projected data were then processed with Harmony software. First, nuclei were segmented by thresholding on the DAPI staining. The cell cytoplasms were segmented by thresholding on the 488 Phalloidin staining. CD4⁺ and CD8⁺ T cells were distinguished by thresholding on the CD4 and CD8 stainings. The number of detected cells, cell area, cell width to length, pSLP76, and F-actin mean intensities were extracted separately for the CD4⁺ and CD8⁺ T-cell subsets with Harmony software. The individual values of each parameter were calculated for every single cell (mean per-object), and the mean value stemming from all the cells of each well was also calculated (mean per well). The mean per well values were used from Figs. 1–5F, while mean per-object values were used to construct Fig. 5G, H.

High-content cell imaging of PBMCs from MS patients

Staining. The HCI workflow described above for HD samples was adapted for MS samples with the following modifications. Imaging plates were coated with 1.25 μg/mL VCAM-1. A total of 27,000 cells were seeded in each well and stimulated for 10 min at 37 °C, before fixation. Cells were stained overnight at 4 °C with 1:500 α-pSLP76 antibody (Rabbit ab75829), 1:500 Phalloidin 488 (A12379) and either 1:500 α-CD4 antibody (IgG2a MAB3791), or α-CD8 antibody (IgG2a MAB3803), or α-CD14 antibody (IgG2a MCA1568T), or α-CD19 antibody (IgG1 MAB4867). The secondary staining step consisted of 1:200 α-rabbit Alexa 647 (A21245), 1:100 DAPI and either 1:200 α-IgG1 Alexa 546 (A21123) or α-IgG2a Alexa 546 (A21133).

Image acquisition. Plates were subjected to two rounds of confocal imaging with a 20 × 0.4 NA Plan Apochromat air objective (25 fields-of-view covering the entire well) and a 63 × 1.15 NA Plan Apochromat water immersion objective (56 fields-of-view). The subpopulations of PBMCs were segregated by thresholding for the staining intensity of the relevant staining (CD4 for CD4⁺ T cells, CD8 for CD8⁺ T cells, CD14 for monocytes and CD19 for B cells). Morphological filters (cell and nucleus area) were added to further distinguish lymphocytes from monocytes. Once the subsets were identified, basic morphological and intensity parameters were extracted with Harmony software. For the images acquired with the 63x objective, the analysis was enriched by applying the SER and STAR methods of Harmony on the F-actin and pSLP76 stainings. This resulted in a library of 407 features.

Under-agarose migration of CD8⁺ T cells from MS patients

A 384-well plate was coated with VCAM-1 (0.625 μg/mL) at 4 °C overnight, then rinsed with PBS before cell culture medium was added to accommodate the cells. To produce a confined environment, a 50 μL layer of 0.5% agarose in RPMI was placed in each well used for the

assay. CD8⁺ T cells from four responder patients and four non-responder patients were collected, centrifuged (10 min 122 × g) and resuspended in RPMI. Responders' cells were stained with 1:1000 Calcein Red-Orange and non-responders' cells were stained with 1:500 CellTracker Green CMFDA. After incubation at 37 °C for 30 min and centrifugation, cells were resuspended in RPMI medium containing 5% human serum. Pairs of non-responder/responder cells were formed, mixed gently, and adjusted for a concentration of 25,000 cells from each patient per 10 μL. Natalizumab was added in a final concentration of 2 μg/mL and cells were then injected under the agarose layer. The plate was then incubated for 30 min at 37 °C with 5% CO₂, and the microscope's (Opera Phenix, Perkin Elmer) temperature and CO₂ levels were adjusted accordingly. An 8-h acquisition phase followed, capturing images of the entire well at 1-min intervals at 10x magnification. The resulting images from the first 2 h were then processed using the cell tracking tool from Harmony software, and validated by the TrackMate tool in ImageJ, to extract relevant cell motility parameters, allowing for the accurate quantification of cell migration.

Imaging of patient T cells treated with actin-disrupting drugs

CD8⁺ T cells were isolated from two responder patients and two non-responder patients. Cells were pretreated with natalizumab and stimulated on VCAM-1-coated imaging plates as described above. After 10 min stimulation, cells were treated with Latrunculin B or Jasplakinolide at a final concentration of 0.25 μM for 10 min or were left untreated. Following treatment, cells were fixed and permeabilized as described above and stained overnight at 4 °C with 1:500 Phalloidin (A12379), 1:500 α-ArpclB antibody (ab99314), and 1:500 α-αTubulin antibody (T6199). A secondary incubation was performed using species-specific secondary antibodies. Imaging was conducted using the Opera Phenix confocal microscope with a 63x magnification objective.

Statistical information

Replicates and data treatment. All imaging experiments were conducted with technical and independent replicates. The technical replicates consist of different wells for analysis of the same condition on the same 384-well plate, while the biological replicates consist of independent experiments performed on different days and/or by different experimenters. The number and type of replicates are described in each figure legend. The data shown in the graphs represent the average of the replicates of each condition, which is available in the Data Source. Consistency among the replicates was checked across the datasets.

Unsupervised analysis for sample discrimination based on natalizumab therapy response. The unsupervised analyses were performed using XLSTAT Basic 2022.5.1. The PCA was done using a correlation (Pearson) type, with a maximum of five calculated components. The chosen component was based on the highest % to explain system variability. The K-mean clustering was calculated using Euclidean distance dissimilarity index, Determinant (W) clustering criterion, with a maximum of ten clusters. The number of clusters selected to explain the results was based on the highest Silhouette score. To validate the number of clusters pointed by the silhouette scores, hierarchical ascendent classification was also performed. The clustering was considered only if both analyses led to the same result. The chi-squared test was applied to confirm the composition difference between the two clusters. The Ward clustering and the heatmap representation were generated by the SRPLOT server based on the 50 features that most contributed to explain the segregation through the F1 component of the PCA.

Machine learning-based analysis for feature combination in natalizumab therapy response. A random forest classifier (RFC) was embedded in the Scikit-learn Python library v1.2.0⁴⁹. We independently analyzed the 407 features from both the discovery and validation

cohorts. The datasets were split into 70:30 training and test samples for the first ($n=28:12$) and second ($n=18:9$) cohorts, while ensuring a stratified distribution of the classes. For each unique combination of features, we trained a separate RFC model. The RFC hyperparameters for each model were tuned using the GridSearchCV function with 20-fold cross-validation. The evaluation focused on combinations with the highest F1 score. To remove redundancies, we removed features having >90% correlation, leading us to retain 133 features in the first cohort. We subsetted the second cohort with the most important features selected on the first cohort to train individual models for each combination, subsequently evaluating their performance metrics. To state prediction performance, we focused on combination trees that achieved an F1 score of $\geq 85\%$ in the discovery and validation cohorts. This cut-off discards combinations leading to maximum prediction performance with features that are not common and consistent across cohorts. Although there is a drop in prediction performance, the applied cut-off ensures robustness of prediction, reinforces feature relevance for distinguishing responders from non-responders, and reduces the probability of overfitting.

Statistical analysis and graphical representations. Normality tests were applied before statistical tests have been performed; thus, each statistical test corresponds to the type of sample distribution. All statistical tests performed were two-sided. To evaluate the effect of natalizumab on cell adhesion, morphology, F-actin, and pSLP76 intensity, we calculated the means of the corresponding cell values among the replicates for each donor. The means for the conditions, untreated and natalizumab exposed, for each donor were plotted and compared. Statistical differences between the paired means were determined through paired *t*-tests. Differences between the untreated means and natalizumab-exposed were considered significant if the calculated *t*-tests *p* values were under 0.05.

To assess how natalizumab distinctly affects responders and non-responder cells in morphology or actin-related features, the means of the corresponding relative delta among the replicates for each donor were obtained. The relative delta is calculated for each donor as: mean of untreated condition – mean of natalizumab condition/mean of untreated condition $\times 100$, for each donor. The means for the responders and non-responders for each donor were plotted and compared. Statistical differences between the unpaired means were determined through an unpaired *t*-test with Welch's correction. Differences between the untreated means and natalizumab-exposed were considered significant if the calculated *t*-tests *p* values were under 0.05.

To determine differences among samples from responders and non-responders treated or not with natalizumab in the context of cell migration and response to actin inhibitors, we calculated the means of the corresponding cell values among the replicates for each donor in the respective experiments. The means were plotted and compared. To determine statistical differences among this set of means, Tukey's multiple comparison tests were applied to features following a normal distribution (migration experiments, Fig. 5D–F) and Dunn's test to features not normally distributed (actin inhibition, Fig. 5G, H). *P* values under 0.05 were considered significant.

Graphs and statistical analysis were generated with GraphPad Prism v8.0.2.

Reporting summary

Further information on research design is available in the Nature Portfolio Reporting Summary linked to this article.

Data availability

Complementary data are included in the Supplementary Information. Flow cytometry and image datasets are located in controlled access data storage at the INSERM Infinity Institute and will be made available upon request. The raw numbers for charts and graphs are available in

the Source Data file. Additional information and requests for resources should be directed to and will be fulfilled by the lead contact, Loïc Dupré (loic.dupre@inserm.fr). Source data are provided with this paper.

Code availability

The code used to apply a random forest-based approach to investigate whether samples from responder and non-responder patients could be distinguished is provided with this paper. It can be accessed with the following link: https://github.com/csbl-br/natalizumab_ML.

References

1. Hemler, M. E., Elices, M. J., Parker, C. & Takada, Y. Structure of the integrin VLA-4 and its cell-cell and cell-matrix adhesion functions. *Immunol. Rev.* **114**, 45–65 (1990).
2. Alon, R. et al. The integrin VLA-4 supports tethering and rolling in flow on VCAM-1. *J. Cell Biol.* **128**, 1243–1253 (1995).
3. Mittelbrunn, M. et al. VLA-4 integrin concentrates at the peripheral supramolecular activation complex of the immune synapse and drives T helper 1 responses. *Proc. Natl Acad. Sci. USA* **101**, 11058–11063 (2004).
4. Nguyen, K., Sylvain, N. R. & Bunnell, S. C. T cell costimulation via the integrin VLA-4 inhibits the actin-dependent centralization of signaling microclusters containing the adaptor SLP-76. *Immunity* **28**, 810–821 (2008).
5. Kim, T. K., Billard, M. J., Wieder, E. D., McIntyre, B. W. & Komanduri, K. V. Co-engagement of alpha(4)beta(1) integrin (VLA-4) and CD4 or CD8 is necessary to induce maximal Erk1/2 phosphorylation and cytokine production in human T cells. *Hum. Immunol.* **71**, 23–28 (2010).
6. Pyka-Fościak, G., Lis, G. J. & Litwin, J. A. Adhesion molecule profile and the effect of anti-VLA-4 mAb treatment in experimental autoimmune encephalomyelitis, a mouse model of multiple sclerosis. *Int J. Mol. Sci.* **23**, 4637 (2022).
7. Elovaara, I. et al. Adhesion molecules in multiple sclerosis: relation to subtypes of disease and methylprednisolone therapy. *Arch. Neurol.* **57**, 546–551 (2000).
8. Schläger, C. et al. Effector T-cell trafficking between the leptomeninges and the cerebrospinal fluid. *Nature* **530**, 349–353 (2016).
9. Schneider-Hohendorf, T. et al. VLA-4 blockade promotes differential routes into human CNS involving PSL-1 rolling of T cells and MCAM-adhesion of TH17 cells. *J. Exp. Med.* **211**, 1833 (2014).
10. Charabati, M. et al. DICAM promotes TH17 lymphocyte trafficking across the blood-brain barrier during autoimmune neuroinflammation. *Sci. Transl. Med.* **14**, eabj0473 (2022).
11. Yednock, T. A. et al. Prevention of experimental autoimmune encephalomyelitis by antibodies against $\alpha 4\beta 1$ integrin. *Nature* **356**, 63–66 (1992).
12. Yang, G. X. & Hagmann, W. K. VLA-4 antagonists: potent inhibitors of lymphocyte migration. *Med. Res. Rev.* **23**, 369–392 (2003).
13. Schwab, N. & Wiendl, H. Learning CNS immunopathology from therapeutic interventions. *Sci. Transl. Med.* **15**, eadg7863 (2023).
14. Polman, C. H. et al. A randomized, placebo-controlled trial of natalizumab for relapsing multiple sclerosis. *N. Engl. J. Med.* **354**, 899–910 (2006).
15. Martin-Blondel, G. et al. Migration of encephalitogenic CD8 T cells into the central nervous system is dependent on the $\alpha 4\beta 1$ -integrin. *Eur. J. Immunol.* **45**, 3302 (2015).
16. Havrdova, E. et al. Effect of natalizumab on clinical and radiological disease activity in multiple sclerosis: a retrospective analysis of the natalizumab safety and efficacy in relapsing-remitting multiple sclerosis (AFFIRM) study. *Lancet Neurol.* **8**, 254–260 (2009).
17. Prosperini, L., Fanelli, F. & Pozzilli, C. Long-term assessment of no evidence of disease activity with natalizumab in relapsing multiple sclerosis. *J. Neurol. Sci.* **364**, 145–147 (2016).

18. Defer, G. et al. CD49d expression as a promising biomarker to monitor natalizumab efficacy. *J. Neurol. Sci.* **314**, 138–142 (2012).
19. Muñoz, Ú. et al. Serum levels of IgM to phosphatidylcholine predict the response of multiple sclerosis patients to natalizumab or IFN- β . *Sci. Rep.* **12**, 13357 (2022).
20. Balasa, R. et al. The matrix metalloproteinases panel in multiple sclerosis patients treated with natalizumab: a possible answer to natalizumab non-responders. *CNS Neurol. Disord. Drug Targets* **17**, 464–472 (2018).
21. Villar, L. M. et al. Immunological markers of optimal response to natalizumab in multiple sclerosis. *Arch. Neurol.* **69**, 191–197 (2012).
22. Sargent-Freitas, J., Batista, S., MacArio, C., Matias, F. & Sousa, L. Clinical predictors of an optimal response to natalizumab in multiple sclerosis. *J. Clin. Neurosci.* **20**, 659–662 (2013).
23. Bloomgren, G. et al. Risk of natalizumab-associated progressive multifocal leukoencephalopathy. *N. Engl. J. Med.* **366**, 1870–1880 (2012).
24. German, Y. et al. Morphological profiling of human T and NK lymphocytes by high-content cell imaging. *Cell Rep.* **36**, 109318 (2021).
25. Severin, Y. et al. Multiplexed high-throughput immune cell imaging reveals molecular health-associated phenotypes. *Sci. Adv.* **8**, 5631 (2022).
26. Kropivsek, K. et al. Ex vivo drug response heterogeneity reveals personalized therapeutic strategies for patients with multiple myeloma. *Nat. Cancer* **4**, 734–753 (2023).
27. Vicente-Manzanares, M. & Sánchez-Madrid, F. Role of the cytoskeleton during leukocyte responses. *Nat. Rev. Immunol.* <https://doi.org/10.1038/nri1268> (2004).
28. Hyduk, S. J. & Cybulsky, M. I. α 4 Integrin signaling activates phosphatidylinositol 3-kinase and stimulates T cell adhesion to intercellular adhesion molecule-1 to a similar extent as CD3, but induces a distinct rearrangement of the actin cytoskeleton. *J. Immunol.* **168**, 696–704 (2002).
29. Outteryck, O. et al. A prospective observational post-marketing study of natalizumab-treated multiple sclerosis patients: clinical, radiological and biological features and adverse events. The BIO-NAT cohort. *Eur. J. Neurol.* **21**, 40–48 (2014).
30. Pulido, R. et al. Functional evidence for three distinct and independently inhibitable adhesion activities mediated by the human integrin VLA-4. Correlation with distinct α 4 epitopes. *J. Biol. Chem.* **266**, 10241–10245 (1991).
31. Malani, D. et al. Implementing a functional precision medicine tumor board for acute myeloid leukemia. *Cancer Discov.* **12**, 388–401 (2022).
32. Snijder, B. et al. Image-based ex-vivo drug screening for patients with aggressive haematological malignancies: interim results from a single-arm, open-label, pilot study. *Lancet Haematol.* **4**, e595–e606 (2017).
33. Kornauth, C. et al. Functional precision medicine provides clinical benefit in advanced aggressive hematologic cancers and identifies exceptional responders. *Cancer Discov.* **12**, 372–387 (2022).
34. Granell-Geli, J. et al. Assessing blood-based biomarkers to define a therapeutic window for natalizumab. *J. Pers. Med.* **11**, 1347 (2021).
35. Xu, Z., Guo, K., Chu, W., Lou, J. & Chen, C. Performance of machine learning algorithms for predicting adverse outcomes in community-acquired pneumonia. *Front. Bioeng. Biotechnol.* **10**, 1 (2022).
36. El-Bouri, W. K., Sanders, A. & Lip, G. Y. H. Predicting acute and long-term mortality in a cohort of pulmonary embolism patients using machine learning. *Eur. J. Intern. Med.* <https://doi.org/10.1016/J.EJIM.2023.07.012> (2023).
37. Kavaka, V. et al. Twin study identifies early immunological and metabolic dysregulation of CD8+ T cells in multiple sclerosis. *Sci. Immunol.* **9**, eadj8094 (2024).
38. Beldi-Ferchiou, A. et al. High effector-memory CD8+ T-cell levels correlate with high PML risk in natalizumab-treated patients. *Mult. Scler. Relat. Disord.* **46**, 102470 (2020).
39. Dallari, S. et al. Upregulation of integrin expression on monocytes in multiple sclerosis patients treated with natalizumab. *J. Neuroimmunol.* **287**, 76–79 (2015).
40. Mellergård, J. et al. Increased B cell and cytotoxic NK cell proportions and increased T cell responsiveness in blood of natalizumab-treated multiple sclerosis patients. *PLoS ONE* **8**, e81685 (2013).
41. Roy, N. H. et al. LFA-1 signals to promote actin polymerization and upstream migration in T cells. *J. Cell Sci.* **133**, jcs248328 (2020).
42. Papayannopoulou, T., Priestley, G. V. & Nakamoto, B. Anti-VLA4/VCAM-1-Induced mobilization requires cooperative signaling through the kit/mkit ligand pathway. *Blood* **91**, 2231–2239 (1998).
43. Ley, K., Rivera-Nieves, J., Sandborn, W. J. & Shattil, S. Integrin-based therapeutics: biological basis, clinical use and new drugs. *Nat. Rev. Drug Discov.* <https://doi.org/10.1038/nrd.2015.10> (2016).
44. Dupré, L., Houmadi, R., Tang, C. & Rey-Barroso, J. T lymphocyte migration: an action movie starring the actin and associated actors. *Front. Immunol.* **6**, 586 (2015).
45. Rullo, J. et al. Actin polymerization stabilizes α 4 β 1 integrin anchors that mediate monocyte adhesion. *J. Cell Biol.* **197**, 115–129 (2012).
46. Alzubaidi, L. et al. Review of deep learning: concepts, CNN architectures, challenges, applications, future directions. *J. Big Data* **8**, 1–74 (2021).
47. Hittle, M. et al. Population-based estimates for the prevalence of multiple sclerosis in the United States by race, ethnicity, age, sex, and geographic region. *JAMA Neurol.* **80**, 693–701 (2023).
48. Havrdova, E., Galetta, S., Stefoski, D. & Comi, G. Freedom from disease activity in multiple sclerosis. *Neurology* **74**, S3–S7 (2010).
49. Pedregosa, F. et al. Scikit-learn: machine learning in Python. *J. Mach. Learn. Res.* **12**, 2825–2830 (2011).

Acknowledgements

We thank Astrid Canivet and David Sagnat from the Organoïd facility of the Institut de Recherche en Santé Digestive (IRSD) for assistance with image acquisition. We thank Mathieu Fusaro and Pierre-Emmanuel Paulet (INFINITy) for their support with Healthy Donors samples. We thank Clémence Bolut for the graph design. This work was supported by Brazilian Federal Agency for Support and Evaluation of Graduate Education (CAPES, grant numbers CAPES-PRINT – 88887.571313/2020-00) to B.C., and by research grants from the Brazilian Research Council (CNPq) and the Rio de Janeiro Research Council (FAPERJ) to V.C.-d.-A., the São Paulo State Research Foundation (FAPESP, grant numbers 2018/14933-2 to H.N.; 2019/27139-5 to J.C.S.S.), the French MS society (ARSEP) to R.L. and B.C., the French National Centre for Scientific Research (CNRS, International Research Project SystAct to L.D.) and the French National Institute of Health and Medical Research (Inserm, International Research Project AdaptAct to L.D.). The funders had no role in study design, data collection and analysis, decision to publish, or preparation of the manuscript.

Author contributions

B.C. contributed to the design of the research, performed experiments, designed the analytical pipeline, analyzed data, and wrote the paper; J.S.S., H.N., and M.A. supervised analysis and built the predictive models; F.B. contributed to patient sample management and patient data collection; N.S.-J., G.P., C.L., and S.K. performed experiments; A.L.A., M.M., and J.S. participated in scientific discussions; R.L. participated in research design and scientific discussions; V.C.-d.-A. and L.D. designed the research, supervised the analysis pipeline, and wrote the paper.

Competing interests

The authors declare no competing interests.

Additional information

Supplementary information The online version contains supplementary material available at
<https://doi.org/10.1038/s41467-025-60224-3>.

Correspondence and requests for materials should be addressed to Vinicius Cotta-de-Almeida or Loïc Dupré.

Peer review information *Nature Communications* thanks Johan Meller-gård and the other anonymous reviewer(s) for their contribution to the peer review of this work. A peer review file is available.

Reprints and permissions information is available at
<http://www.nature.com/reprints>

Publisher's note Springer Nature remains neutral with regard to jurisdictional claims in published maps and institutional affiliations.

Open Access This article is licensed under a Creative Commons Attribution-NonCommercial-NoDerivatives 4.0 International License, which permits any non-commercial use, sharing, distribution and reproduction in any medium or format, as long as you give appropriate credit to the original author(s) and the source, provide a link to the Creative Commons licence, and indicate if you modified the licensed material. You do not have permission under this licence to share adapted material derived from this article or parts of it. The images or other third party material in this article are included in the article's Creative Commons licence, unless indicated otherwise in a credit line to the material. If material is not included in the article's Creative Commons licence and your intended use is not permitted by statutory regulation or exceeds the permitted use, you will need to obtain permission directly from the copyright holder. To view a copy of this licence, visit <http://creativecommons.org/licenses/by-nc-nd/4.0/>.

© The Author(s) 2025

Terms and Conditions

Springer Nature journal content, brought to you courtesy of Springer Nature Customer Service Center GmbH (“Springer Nature”). Springer Nature supports a reasonable amount of sharing of research papers by authors, subscribers and authorised users (“Users”), for small-scale personal, non-commercial use provided that all copyright, trade and service marks and other proprietary notices are maintained. By accessing, sharing, receiving or otherwise using the Springer Nature journal content you agree to these terms of use (“Terms”). For these purposes, Springer Nature considers academic use (by researchers and students) to be non-commercial.

These Terms are supplementary and will apply in addition to any applicable website terms and conditions, a relevant site licence or a personal subscription. These Terms will prevail over any conflict or ambiguity with regards to the relevant terms, a site licence or a personal subscription (to the extent of the conflict or ambiguity only). For Creative Commons-licensed articles, the terms of the Creative Commons license used will apply.

We collect and use personal data to provide access to the Springer Nature journal content. We may also use these personal data internally within ResearchGate and Springer Nature and as agreed share it, in an anonymised way, for purposes of tracking, analysis and reporting. We will not otherwise disclose your personal data outside the ResearchGate or the Springer Nature group of companies unless we have your permission as detailed in the Privacy Policy.

While Users may use the Springer Nature journal content for small scale, personal non-commercial use, it is important to note that Users may not:

1. use such content for the purpose of providing other users with access on a regular or large scale basis or as a means to circumvent access control;
2. use such content where to do so would be considered a criminal or statutory offence in any jurisdiction, or gives rise to civil liability, or is otherwise unlawful;
3. falsely or misleadingly imply or suggest endorsement, approval , sponsorship, or association unless explicitly agreed to by Springer Nature in writing;
4. use bots or other automated methods to access the content or redirect messages
5. override any security feature or exclusionary protocol; or
6. share the content in order to create substitute for Springer Nature products or services or a systematic database of Springer Nature journal content.

In line with the restriction against commercial use, Springer Nature does not permit the creation of a product or service that creates revenue, royalties, rent or income from our content or its inclusion as part of a paid for service or for other commercial gain. Springer Nature journal content cannot be used for inter-library loans and librarians may not upload Springer Nature journal content on a large scale into their, or any other, institutional repository.

These terms of use are reviewed regularly and may be amended at any time. Springer Nature is not obligated to publish any information or content on this website and may remove it or features or functionality at our sole discretion, at any time with or without notice. Springer Nature may revoke this licence to you at any time and remove access to any copies of the Springer Nature journal content which have been saved.

To the fullest extent permitted by law, Springer Nature makes no warranties, representations or guarantees to Users, either express or implied with respect to the Springer nature journal content and all parties disclaim and waive any implied warranties or warranties imposed by law, including merchantability or fitness for any particular purpose.

Please note that these rights do not automatically extend to content, data or other material published by Springer Nature that may be licensed from third parties.

If you would like to use or distribute our Springer Nature journal content to a wider audience or on a regular basis or in any other manner not expressly permitted by these Terms, please contact Springer Nature at

onlineservice@springernature.com